nature neuroscience

SUPPLEMENTARY INFORMATION

https://doi.org/10.1038/s41593-017-0053-5

In the format provided by the authors and unedited.

Mutations in *Vps15* perturb neuronal migration in mice and are associated with neurodevelopmental disease in humans

Thomas Gstrein[1], Andrew Edwards[2], Anna Přistoupilová[3,4,5], Ines Leca[1], Martin Breuss[1], Sandra Pilat-Carotta[1], Andi H. Hansen[1], Ratna Tripathy[1], Anna K. Traunbauer[1], Tobias Hochstoeger[1], Gavril Rosoklija[1], Marco Repic[6], Lukas Landler[1], Viktor Stránecký[3], Gerhard Dürnberger[1], Thomas M. Keane[7], Johannes Zuber[1], David J. Adams[7], Jonathan Flint[2], Tomas Honzik[8], Marta Gut[4,5], Sergi Beltran[4,5], Karl Mechtler[1], Elliott Sherr[9], Stanislav Kmoch[3], Ivo Gut[4,5] and David A. Keays[1]*

[1]Institute of Molecular Pathology (IMP), Vienna Biocentre (VBC), Vienna, Austria. [2]Wellcome Trust Center for Human Genetics (WTCHG), Oxford, UK. [3]Institute of Inherited Metabolic Disorders, Charles University, Prague, Czech Republic. [4]CNAG-CRG, Centre for Genomic Regulation (CRG), Barcelona Institute of Science and Technology (BIST), Barcelona, Spain. [5]Universitat Pompeu Fabra (UPF), Barcelona, Spain. [6]Institute for Molecular Biotechnology (IMBA), Vienna, Austria. [7]Wellcome Trust Sanger Institute, Hinxton, Cambridgeshire, UK. [8]Department of Pediatrics and Adolescent Medicine, First Faculty of Medicine, Charles University, Prague, Czech Republic. [9]Institute of Human Genetics, University of California, San Francisco, San Francisco, CA, USA. *e-mail: keays@imp.ac.at

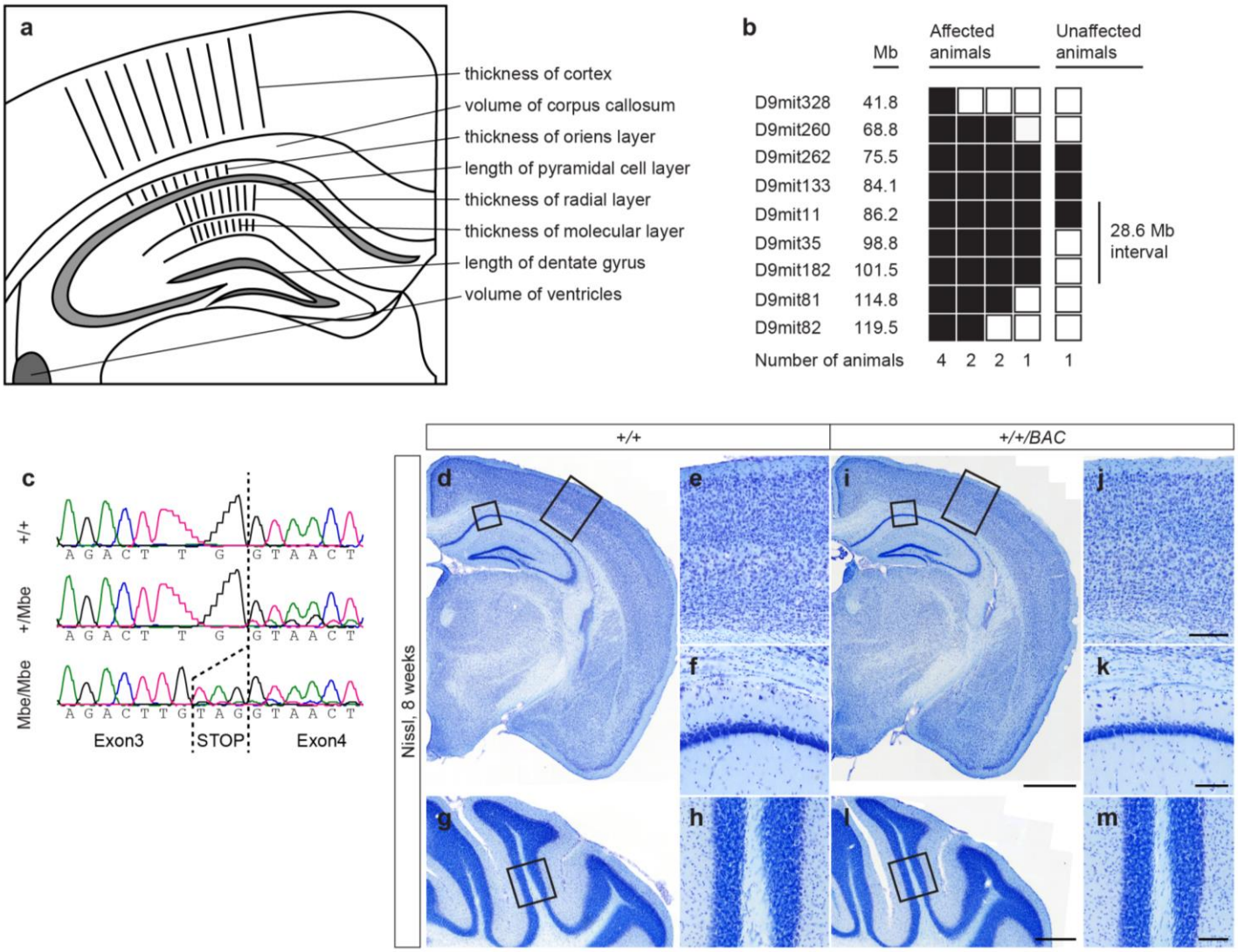

Supplementary Figure 1

Genetic mapping of the Marble mutation.

(a) Schematic showing the parameters assessed for the ENU screen. Nissl stained stereotaxically matched sections through the telencephalon (Bregma -2.06 mm) were analyzed. The following measurements were taken: thickness of the cortex; volume of the corpus callosum; thickness of the stratum oriens of the hippocampus; length of the pyramidal cell layer of the hippocampus; thickness of the radial and molecular layer of the hippocampus; length of the dentate gyrus; and volume of the third ventricle and lateral ventricles. (b) Schematic showing the results for the genetic mapping experiments. The marker and its position along chromosome 9 are shown on the left, and the number of animals with that particular genotype are shown at the bottom. Filled black boxes indicate homozygosity for the ENU mutagenized C57/BL6 allele, whereas clear boxes indicate the presence of at least one C3H/HeH allele. The causative mutation was mapped to a 28.6 Mb interval between D9mit11 and D9mit81. (c). Sequencing traces of *Vps15* cDNA for +/+, *+/Mbe*, *Mbe/Mbe*. mRNA was extracted from the developing forebrain of animals at E14.5, and cDNA generated by reverse transcription. In *Mbe/Mbe* animals the insertion of a stop codon (TAG) can be seen. (d-m) Representative Nissl stains of brains of adult +/+ and *+/+/BAC* mice (n=3 animals per genotype). No structural brain abnormalities were observed in *+/+/BAC* transgenic mice harboring additional copies of Vps15 (i-m) in comparison to littermate wild-type controls (d-h). Boxed areas in (d) and (i) highlight the cortex (magnified in (e) and (j)) and the CA1 region of the hippocampus (magnified in (f) and (k)). (g) and (l) show the cerebellum. Boxed areas are magnified in (h) and (m). The scale bars in (i) show 1000 μm, 200 μm in (j), 100 μm in (k) and (m) and 500 μm in (l).

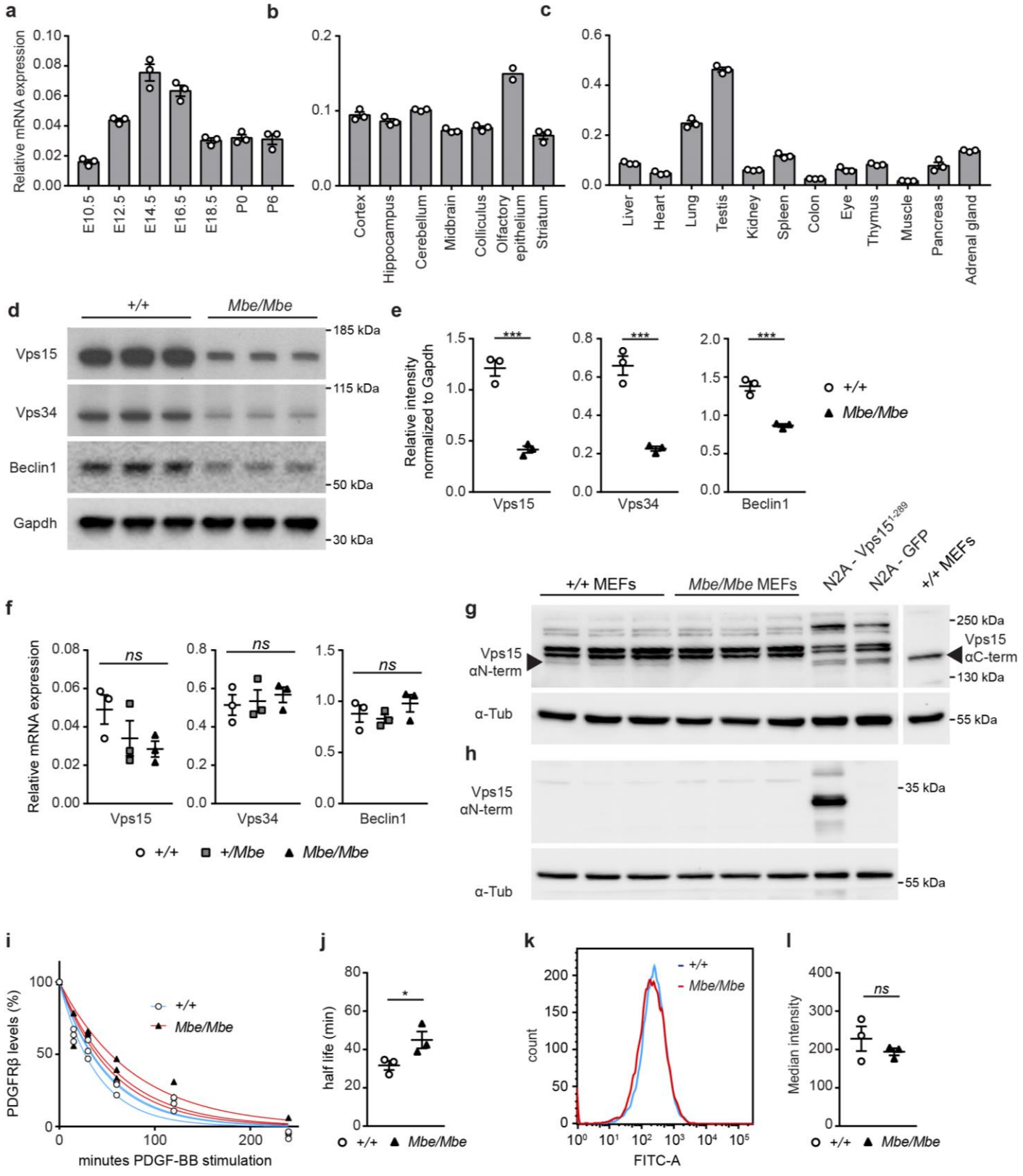

Supplementary Figure 2

Expression of Vps15 and functional analysis of the Marble mutation.

(a-c) qPCR results showing the expression of *Vps15* in: (a) the developing mouse brain from E10.5 to P6; (b) in the adult mouse brain; and (c) in the major organs of the adult mouse. *Vps15* was expressed in all tissues analyzed (n=2-3 technical replicates on a pooled sample of 3 biological samples). (d) Western blot analysis of Vps15, Vps34 and Beclin1 levels in MEFs taken from +/+ and *Mbe/Mbe* animals. Cropped images are shown. Gapdh was employed as a loading control. (e) Relative quantitation of the protein levels shown in (d) reveals a significant reduction in Vps15 (n=3 animal per genotype; one-tailed unpaired t-test, t_4=9.467; P=0.0003), Vps34 (n=3 animals per genotype; one-tailed unpaired t-test, t_4=8.44; P=0.0005), and Beclin1 in *Mbe/Mbe* mutants (n=3 animals per genotype; one-tailed unpaired t-test, t_4=7.877; P=0.0007). (f) qPCR results for transcript levels of *Vps15*, *Vps34* and *Beclin1* from E14.5 brains. While the transcript levels of *Vps15* are lower, there are no significant differences between genotypes (n=3 animals per genotype; one-way ANOVA with a Tukey's multiple comparison; +/+ vs *Mbe/Mbe*: *Vps15*: P=0.1911; Vps34: P=0.7545; Beclin1: P=0.6128) (g-h) Western blot analysis of Vps15 employing a N-terminal antibody in MEFs and Neuro2A (N2A) cells. Cropped images are shown. N2A cells were transfected with a shortened version of Vps15 (1-289) reflecting the predicted length of the *Mbe/Mbe* truncated protein. (g) The N-terminal Vps15 antibody detected full-length Vps15 at physiological levels in +/+ MEFs and N2A cells (highlighted with black arrow head). A C-terminal Vps15 antibody confirmed that the band is Vps15. (h) The N-terminal Vps15 antibody binds Vps15(1-289) with high affinity but does not detect a band at the corresponding size in either +/+ or *Mbe/Mbe* MEFs. These data indicate that the *Marble* mutation does not lead to the expression of a truncated protein, most likely due to nonsense mediated decay of the transcript. (i) Levels of PDGFR receptor β after stimulation with receptor ligand PDGF-BB in +/+ (blue line) and *Mbe/Mbe* (red line) MEFs (n=3). (j) PDGF receptor half-life was calculated from fitted data in (i). *Mbe/Mbe* cells show significantly slower receptor degradation (n=3 animals per genotype, one-tailed unpaired t-test, t_4=2.633; P=0.029). (k) Representative FACs plot of MEFs stained with lysotracker for +/+ and *Mbe/Mbe* animals. The Y axis shows the cell count and the intensity of staining is shown on the X axis. (l) Quantitation of lysotracker results reveals no significant difference between +/+ and *Mbe/Mbe* animals (n=3 animals per genotype; unpaired t-test, t_4=1.022; P=0.3645). Error bars show mean +/- standard error of the mean.

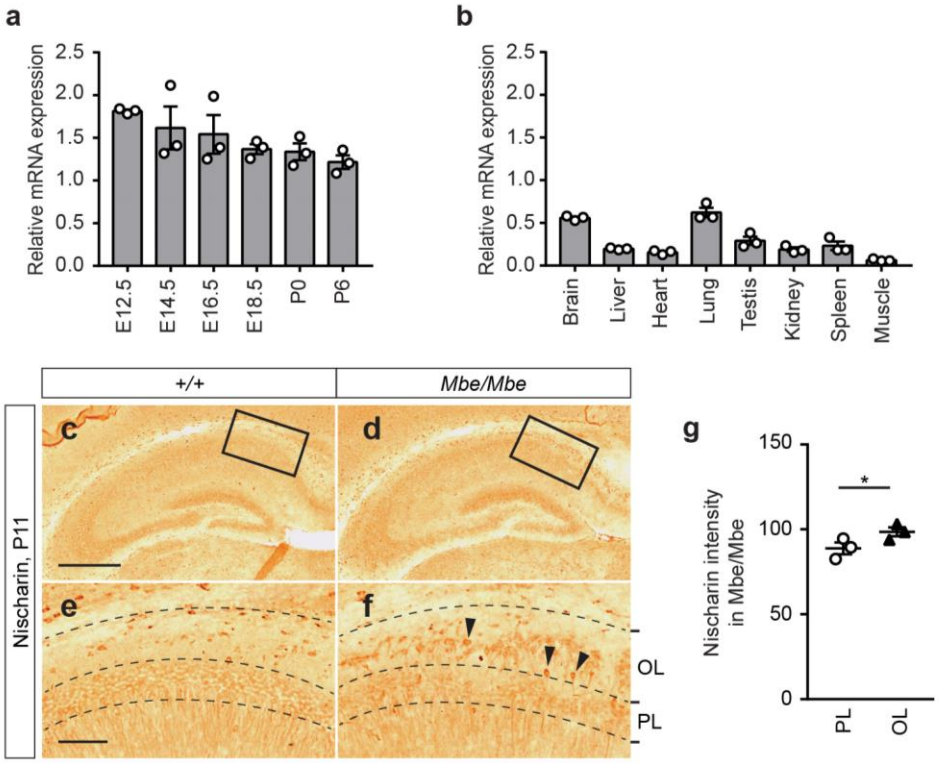

Supplementary Figure 3

Expression analysis of Nischarin.

(a-b) qPCR results showing the expression of *Nischarin* in (a) the developing mouse brain from E12.5 to P6 and (b) in the major organs of the adult mouse (n=3 animals per genotype). *Nischarin* was expressed in all tissues analyzed, with highest expression levels in the developing brain (E12.5 to E16.5). (c-f) Representative images of P11 mouse brains stained with sera against Nischarin. Boxed areas in (c) and (d) are magnified in (e) and (f). Pyramidal neurons located in the oriens layer (OL) were notable for the strong Nischarin staining (black arrow heads). (g) Quantification revealed significantly higher *Nischarin* staining for cells found in the oriens layer (OL) as compared to those located in the pyramidal cell layer (PL) (n=3 animals per genotype; one-tailed unpaired t-test; t_4=2.212; P=0.0457). The scale bar shows 500 μm in (c) and 100 μm in (e). Error bars show mean +/- standard error of the mean.

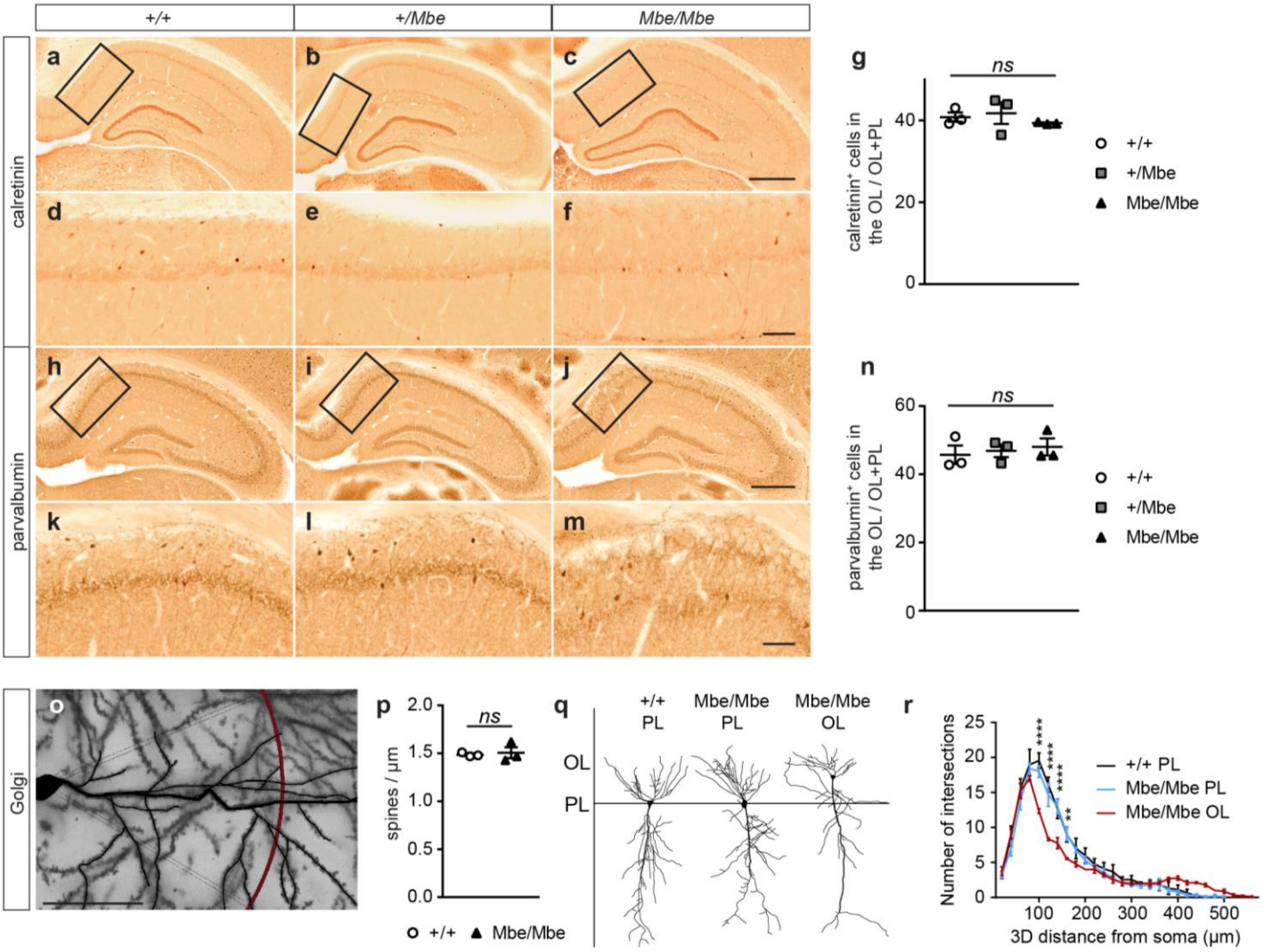

Supplementary Figure 4

Analysis of hippocampal neurons in *Mbe/Mbe* mutants.

(a-m) Representative images of brains from 8-week old mice stained with sera against calretinin (a-f) and parvalbumin (h-m). Quantification showing the percentage of calretinin positive (g) or parvalbumin positive (n) interneurons in the oriens layer (OL). There was no significant difference when comparing *Mbe/Mbe* animals and littermate controls (+/+, *+/Mbe*) (n=3 animals per genotype; calretinin: one-way ANOVA with a Tukey's multiple comparisons test; +/+ vs *Mbe/Mbe*; P=0.8137; parvalbumin: Kruskal-Wallis test with a Dunn's multiple comparison test; +/+ vs *Mbe/Mbe*; P>0.9999). (o) Image of a Golgi stained pyramidal neuron from the hippocampus. Spines located on tertiary apical dendritic branches distanced more than 120µm from the soma (red line) were quantitated. (p) Quantification of spine density in +/+ and *Mbe/Mbe* animals reveals no significant differences between genotypes (n=4-6 neurons per animal; n=3 animals per genotype; two-tailed unpaired t-test; t_4=0.3386; P=0.7519). (q) Schematic representation of CA1 pyramidal neurons that were traced in three dimensions and assessed by Scholl analysis. (r) Quantitation of dendritic intersections from the soma. Ectopic *Mbe/Mbe* neurons exhibit a significant decrease in complexity, that is most evident 100 µm to 160 µm from the soma (n=3 cells per animal, n=3 animals per genotype; two-way ANOVA with a Tukey's multiple comparisons test; interaction P<0.0001, Supplementary Table 1). The scale bars in (c), and (j) show 500 µm, 100 µm in (f) and (m) and 50 µm in (o). Error bars show mean +/- standard error of the mean.

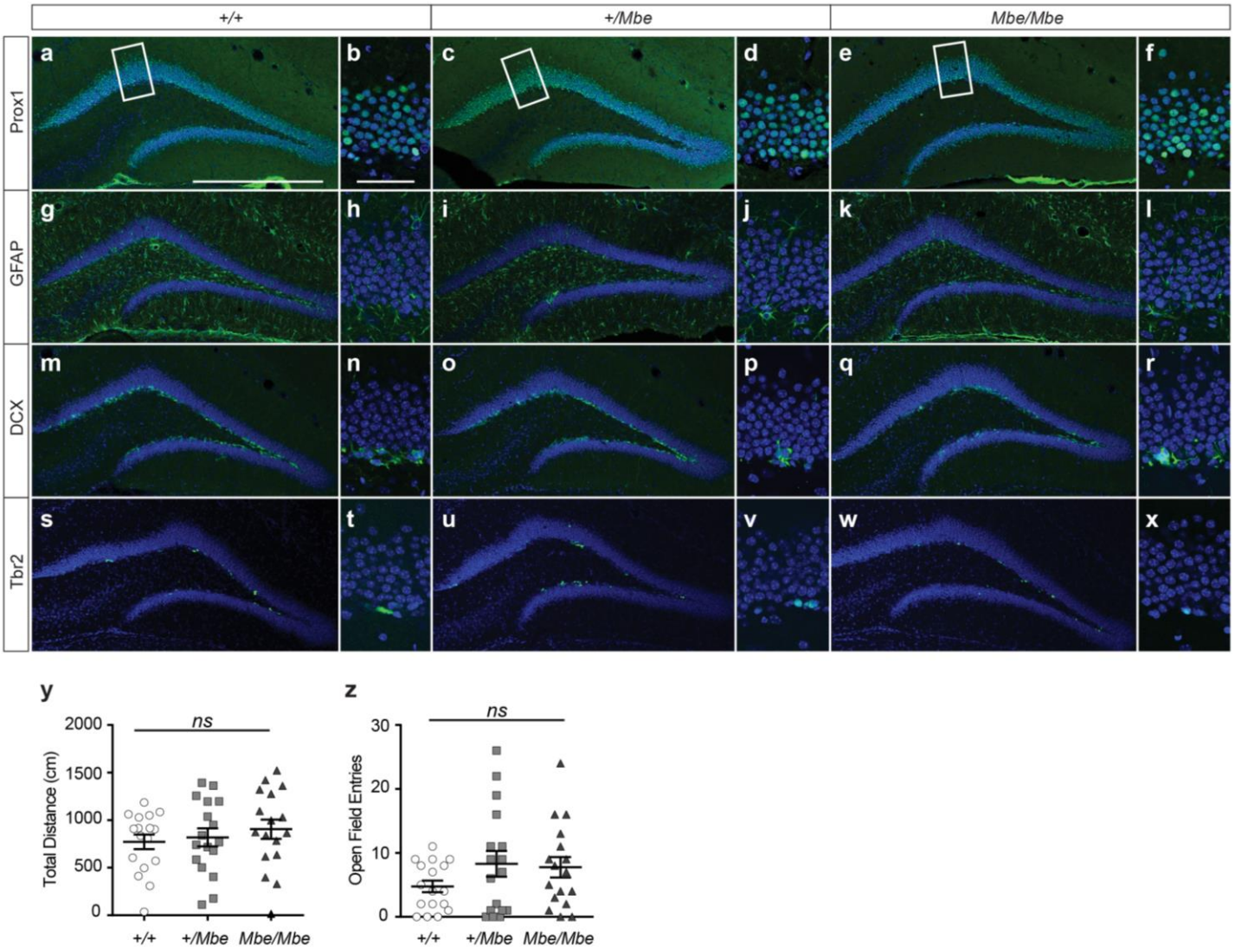

Supplementary Figure 5

The Marble mouse does not show obvious defects in the dentate gyrus nor deficits in locomotion or anxiety.

(a-x) Representative images of histological stainings on the dentate gyrus of adult +/+, +*Mbe*, and *Mbe/Mbe* animals with sera against Prox1 (which labels mature granule cells), GFAP (which labels radial glial-like progenitors), Dcx (which labels newly born neurons), and Tbr2 (which labels intermediate progenitors). These experiments revealed that the granule cell layer and the subgranular zone is similarly organized in all genotypes (n=3 animals per genotype). (y) Total distance travelled in the open field reveals no locomotor phenotype in *Mbe/Mbe* animals (n=17 animals per genotype; one-way ANOVA with a Tukey's multiple comparisons test, Bonferroni corrected; +/+ vs *Mbe/Mbe*; P>0.9999). (z) Number of entries into the center of the open field. There is no significant difference between genotypes indicating anxiety phenotypes are normal in *Mbe/Mbe* animals (n=17 animals per genotype; one-way ANOVA with a Tukey's multiple comparisons test, Bonferroni corrected; +/+ vs *Mbe/Mbe*; P=0.7546). The scale bars show 500 μm in (a) and 100 μm (b). Error bars show mean +/- standard error of the mean.

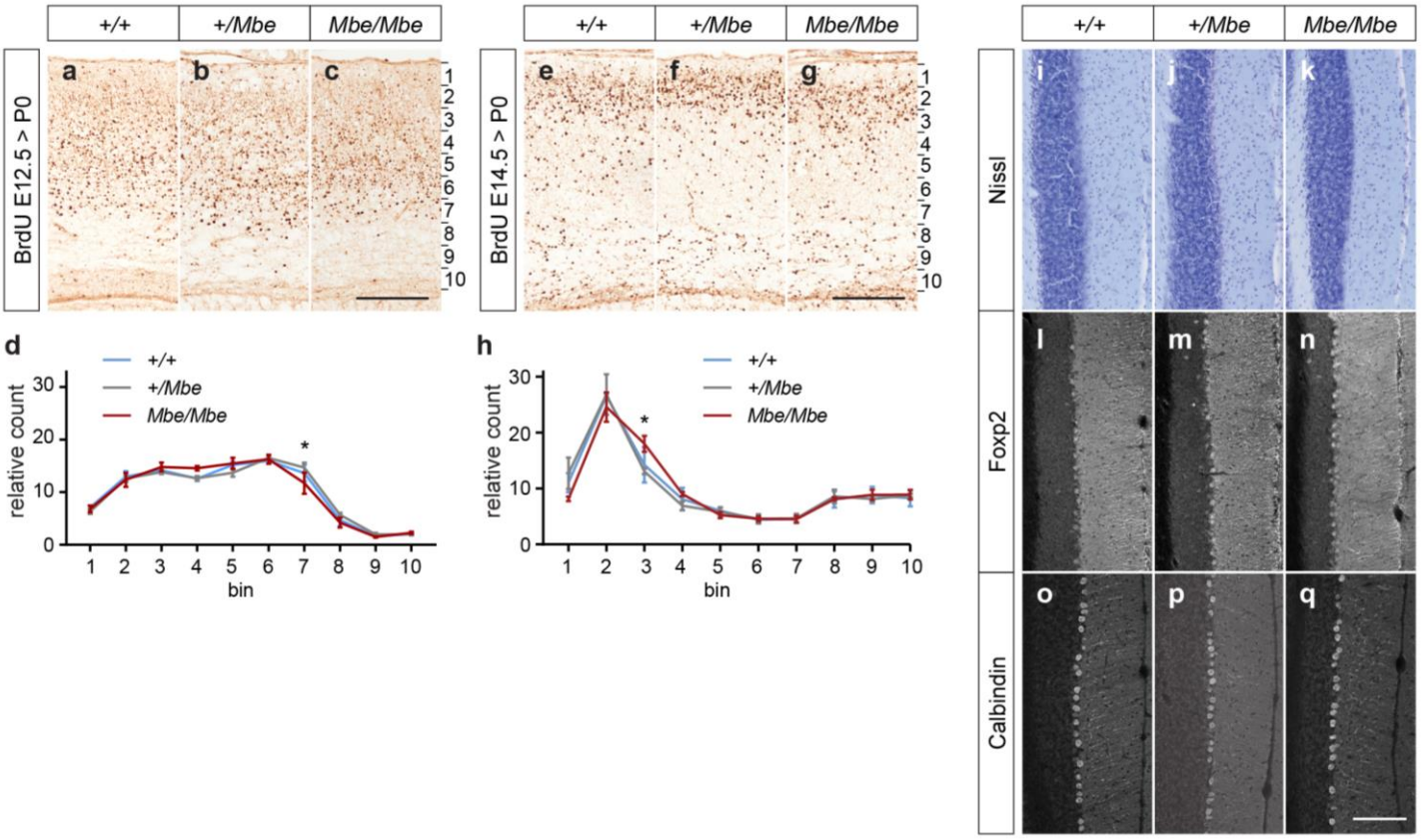

Supplementary Figure 6

Anatomical characterization of the Marble cortex and cerebellum.

(a-g) Representative images of birth date labeling studies following the injection of BrdU in pregnant dams at E12.5 (a-c) and E14.5 (e-g) followed by histological analysis at P0. Cortical sections were divided into ten equal bins, cells counted blind to genotype, and then the relative number of BrdU positive cells calculated for each bin. Bin 10 represents the deepest bin, with bin 1 being closest to the cortical surface. (d, h) Statistical analysis revealed a significant difference when comparing *+/Mbe* heterozygotes with *Mbe/Mbe* mutants at E12.5 in bin 7 (n=5 animals per genotype; two-way repeated measures ANOVA with Tukey's multiple correction test; *+/Mbe* vs *Mbe/Mbe* P=0.0242) and at E14.5 in bin 3 (n=3 animals per genotype; two-way repeated measures ANOVA with Tukey's multiple correction test; *+/Mbe* vs *Mbe/Mbe* P=0.0465). At E14.5 *Mbe/Mbe* mutants have a higher percentage of Brdu positive cells in bin 3 indicative of a mild defect in neuronal migration. Unexpectedly, at E12.5 fewer cells are in bin 7, suggesting mildly faster migration. (i-q) Analysis of the cerebellum in +/+, *+/Mbe*, and *Mbe/Mbe* animals. Panels (i-k) show representative images of Nissl staining, (l-n) Foxp2 staining, and (o-q) Calbindin staining. The molecular layer, Purkinje cell layer, and granule cell layer all appear intact in *Mbe/Mbe* mutants (n=3 animals per genotype). Error bars show mean +/- standard error of the mean. The scale bars in (c) and (g) show 200 μm and 150 μm in (q).

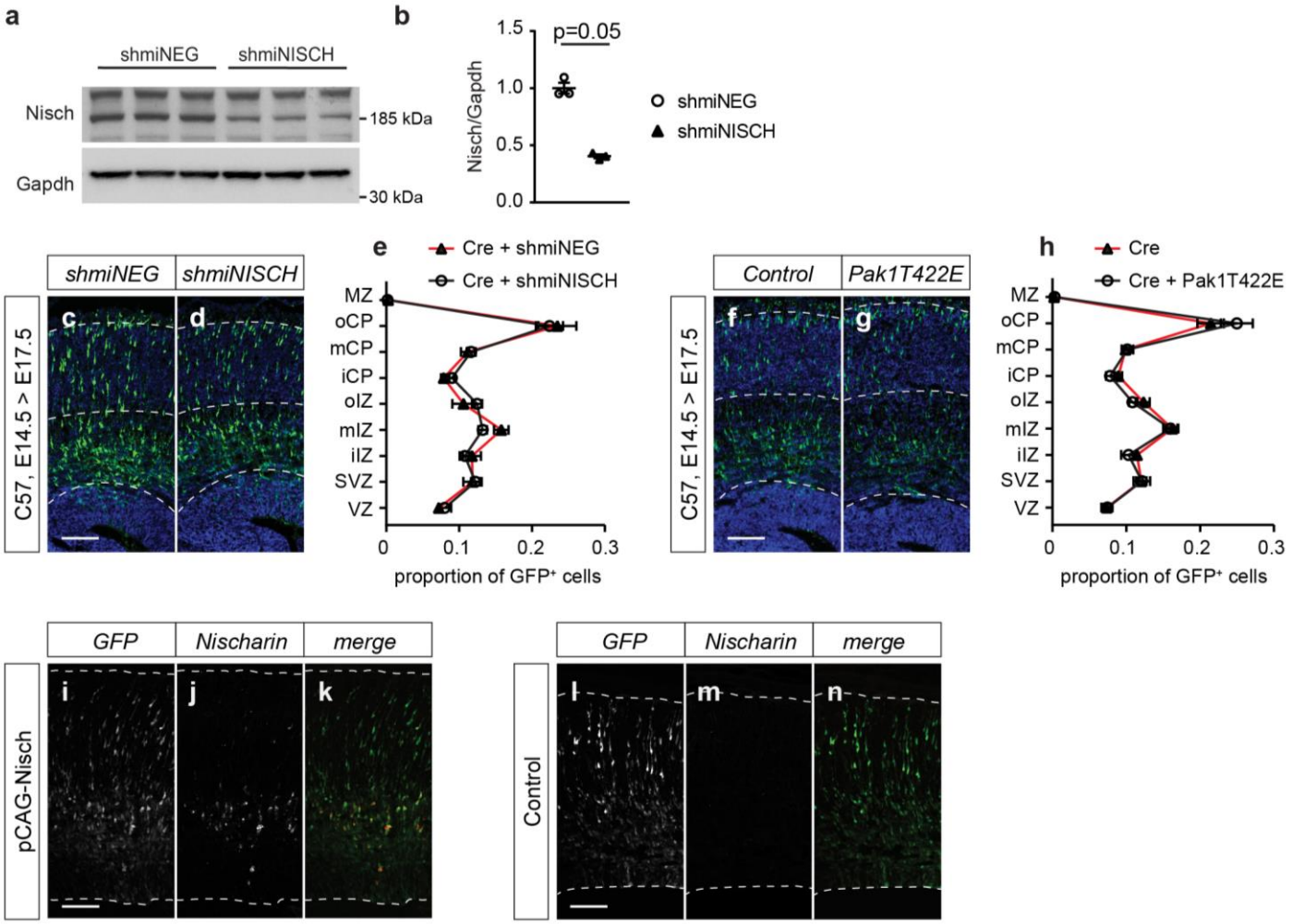

Supplementary Figure 7

Control experiments for in utero electroporation studies.

(a) Western blot analysis of Nischarin in Neuro2A cells transfected with a shmiRNAs targeting Nischarin (shmiNISCH) or a scrambled negative control (shmiNEG). Cropped images are shown. (b) Quantification revealed a 60% reduction in Nischarin protein levels following transfection with a shmiNISCH (n=3 flasks, one-tailed Mann Whitney test; P=0.05). (c-h) Representative images for *in utero* electroporation experiments. Constructs were electroporated at E14.5 before analysis at E17.5. GFP positive cells were quantified in 3 blinded sections per animal in 9 areas across the developing cortex and expressed relative to the total number of cells. (e, h) Electroporation of a knock-down construct targeting Nischarin (c-e) or of a phosphomimetic mutant of Pak1(T422E) (f-h) in wild-type animals did not significantly influence neuronal migration (two-way repeated measures ANOVA with a Bonferroni multiple comparison test; shmiNISCH: n=4 animals per condition, interaction P=0.7074; Pak1(T422E): n=5 animals per condition, interaction P=0.3652). (i-n) Representative images of mouse brains electroporated with either Nischarin or pCAGEN control vector followed by immunostaining with sera targeting Nischarin (n=3 animals per genotype). (i-k) Cells with highest levels of Nischarin congregated in the subventricular and intermediate zones. (l-n) No immunoreactivity for Nischarin was found in mouse brains electroporated with the control vector when employing those imaging conditions used in (i-k). Note that these imaging conditions do not allow detection of the endogenous protein. Error bars show mean +/- standard error of the mean. The scale bar shows 100 μm in (c), (f), (i) and (l).

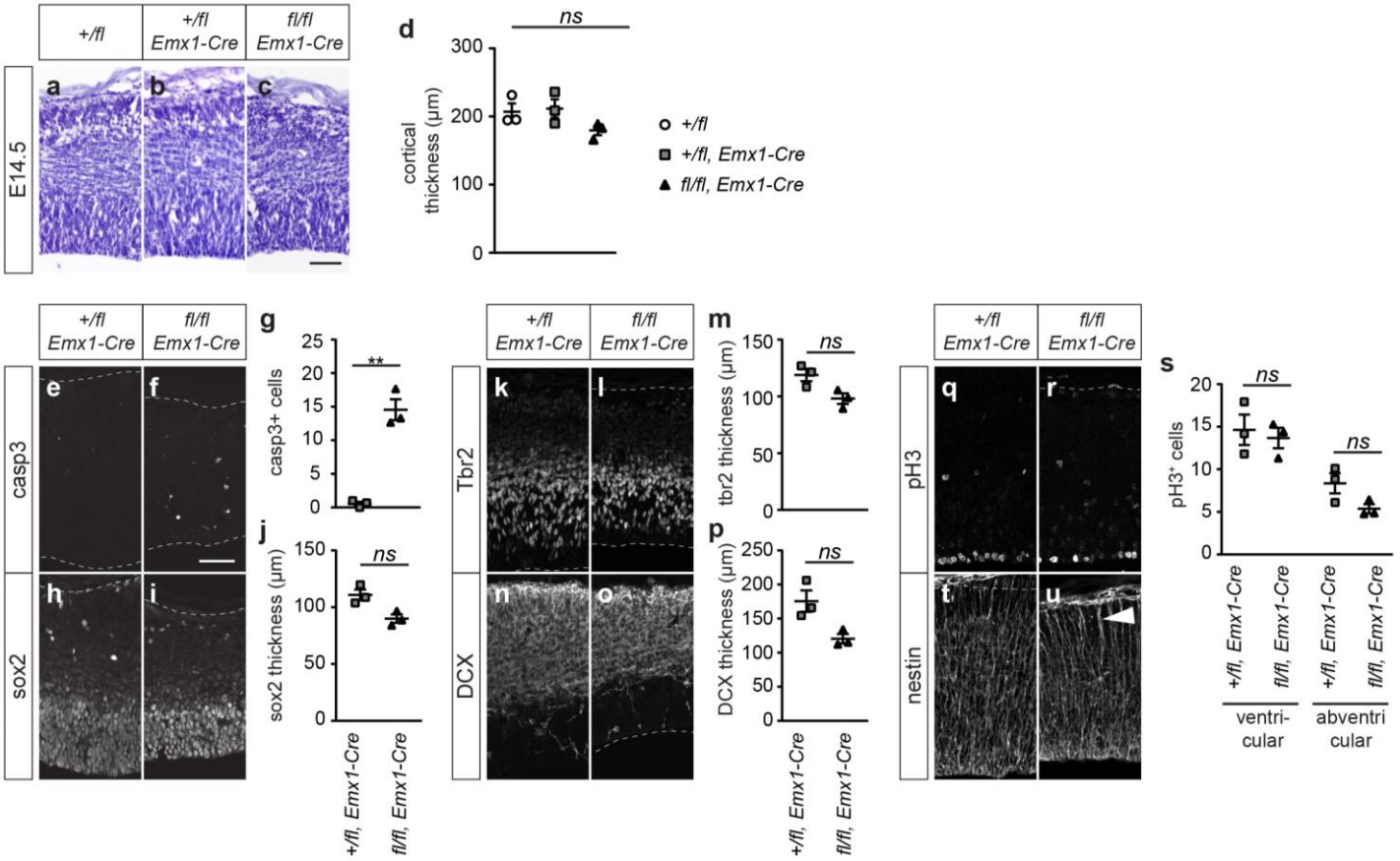

Supplementary Figure 8

Neuroanatomical characterization of *Vps15 fl/fl* Emx1-Cre animals at E14.5.

(a-c) Representative coronal Nissl stains of the developing E14.5 cortex of *+/fl*, *+/fl Emx1-Cre*, and *fl/fl Emx1-Cre* animals. (d) Quantitation of cortical thickness. *fl/fl Emx1-Cre* animals have a thinner cortex, but this is not significantly different from *+/fl* animals (n=3 animals per genotype; Kruskal-Wallis test with a Dunn's correction for multiple testing, Bonferroni corrected; *+/fl* vs *fl/fl Emx1-Cre*; P=0.0714). Analogous to our P0 and P11 results (Figure 6) we did not observe a phenotype in *+/fl Emx1-Cre* heterozygotes. These animals were employed as controls for subsequent stainings. (e-f) Caspase staining of the cortex at E14.5 of *+/fl Emx1-Cre* and *fl/fl Emx1-Cre* animals. Caspase positive cells can be observed in both proliferative and postmitotic regions in *fl/fl Emx1-Cre* animals. (g) Quantification of the number of caspase positive cells reveals a significant difference between genotypes (n=3 animals per genotype; unpaired t-test; one-tailed with a Bonferroni correction; t_4=8.779; P=0.0035). (h-i) Staining with the progenitor marker Sox2 at E14.5 of *+/fl EMX1-Cre* and *fl/fl Emx1-Cre* animals. (j) Quantitation of the thickness of the Sox2 positive layer shows that it is thinner in *fl/fl Emx1-Cre* animals, but this difference is not statistically significant (n=3 animals per genotype; unpaired t-test; one-tailed with a Bonferroni correction; t_4=3.455; P=0.091). (k-l) Staining with the intermediate progenitor marker Tbr2 at E14.5. (m) Quantitation of the thickness of the Tbr2 positive layer, shows that it is thinner in *fl/fl Emx1-Cre* animals, but this difference is not statistically significant (n=3 animals per genotype; unpaired t-test; one-tailed with a Bonferroni correction; t_4=2.867; P=0.1596). (n-o) Staining with the early neuronal marker DCX at E14.5. (p) Quantitation of the thickness of the DCX positive layer shows that it is thinner in *fl/fl Emx1-Cre* animals, but this difference is not statistically significant (n=3 animals per genotype; unpaired t-test; one-tailed with a Bonferroni correction; t_4=3.217; P=0.1134). (q-r) Staining with the M-phase marker pH3 at E14.5. (s) Quantitation of the number of ventricular and abventricular pH3 positive cells reveals a reduction *fl/fl Emx1-Cre* animals, but this difference is not statistically significant (n=3 animals per genotype; two-tailed unpaired t-test; with a Bonferroni correction; abventricular: t_4=2.299; P=0.581; ventricular; t_4=0.4494; P>0.9999). (t-u) Staining with the radial glial marker Nestin at E14.5. Distinct radial glial fibers can be observed in control animals (*+/fl Emx1-Cre)*, in contrast to *fl/fl Emx1-Cre* animals where fibers form thick bundles in the developing cortical plate (shown with an arrow). Images in (a-u) are representative. Scale bars in (c) and (f) show 50 µm. Error bars show mean +/- standard error of the mean.

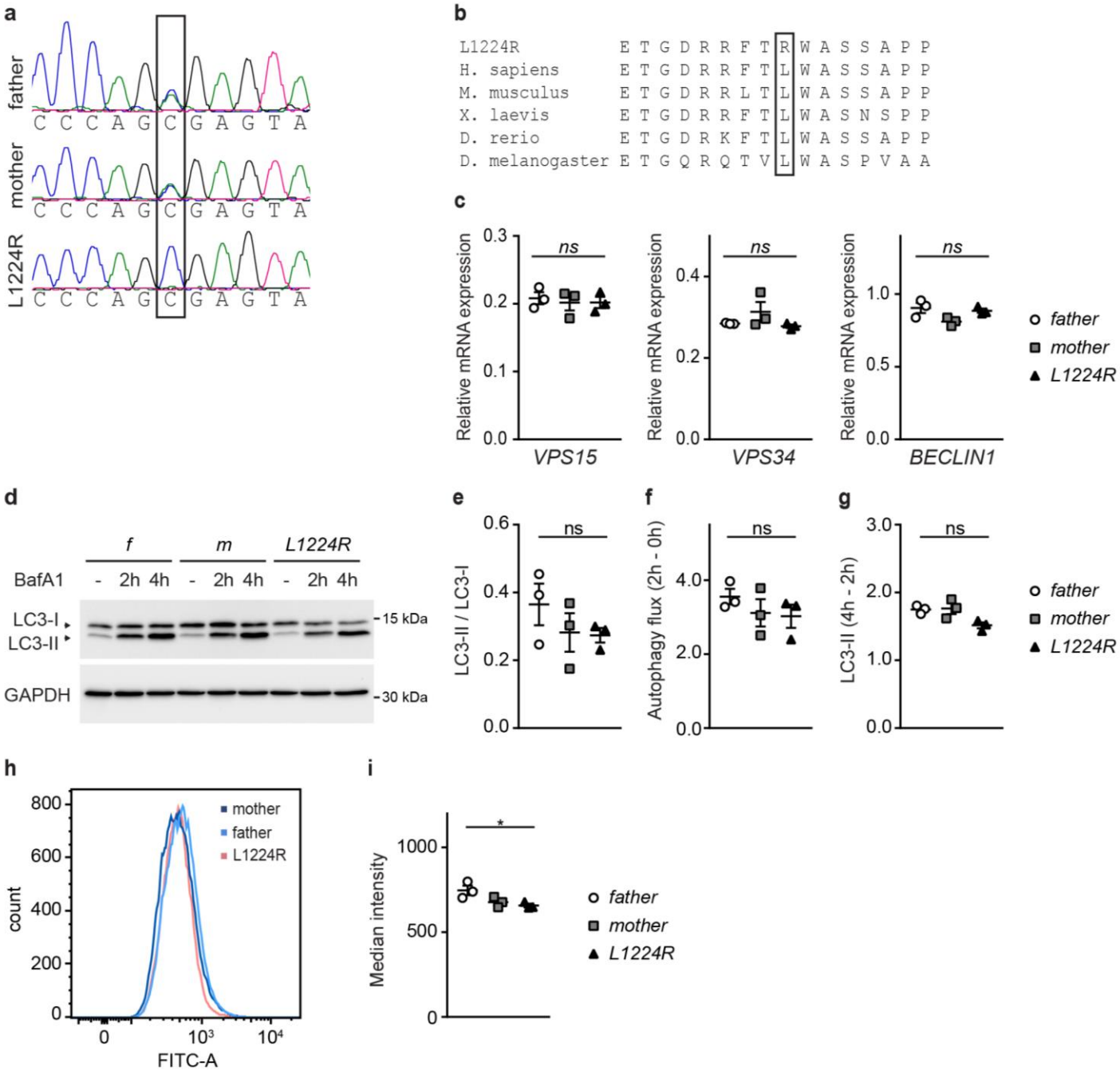

Supplementary Figure 9

Analysis of human dermal fibroblasts obtained from a patient with a L1224R mutation in *VPS15*.

(a) Sequencing traces of the A to C variant in *VPS15* that encodes for a L1224R missense mutation in the homozygous proband. (b) Homology comparison of the L1224 residue in mice, xenopus, zebrafish, and drosophila reveals it is highly conserved. (c) Quantitation of relative mRNA expression of *VPS15*, *VPS34* and *BECLIN1* in dermal fibroblasts from the father, mother and proband. No significant differences were observed on the levels of *VPS15* transcript (n=3 flasks per individual; one-way ANOVA with a Tukey's multiple comparison; father vs proband: P=0.8928; mother vs proband: P=0.9998), on the levels of *VPS34* transcript (n=3 flasks per individual; one-way ANOVA with a Tukey's multiple comparison; father vs proband: P=0.9429; mother vs proband: P=0.2655) or on the levels of *BECLIN1* transcript (n=3 individual flasks; one-way ANOVA with a Tukey's multiple comparison; father vs proband: P=0.8377; mother vs proband: P=0.1506). See Supplementary Table 1. These data indicate the that the reduction in VPS15 protein levels is due to post-

transcriptional dysregulation. (d) Western blot analysis of LC3-I, and LC3-II on protein lysates prepared from patient and parent HDFs before and after lysosomal inhibition with Bafilomycin A1 (n=3 flasks per individual). Cropped images are shown. Quantification (e-g) reveals a reduction in the ratio of LC3-II/LC3-I at 0hrs, but this is not statistically significant (one-way ANOVA with a Tukey's multiple comparison, Bonferroni corrected; father vs proband: P>0.9999, mother vs proband: P>0.9999). Similarly when assessing autophagy flux (2hr-0hr) and formation at (4hr-2h) we observe a reduction in L1224R fibroblasts, however, this is not significant (one-way ANOVA with a Tukey's multiple comparison, Bonferroni corrected; 2hr-0hr: father vs proband: P>0.9999, mother vs proband: P>0.9999; 4hr-2hr: father vs proband: P=0.1836, mother vs proband: P=0.1482). (h) Representative FACs plot for lysotracker experiments conducted on HDFs from the mother (shown in dark blue), father (shown in light blue), and proband (shown in red). The Y axis shows the cell count and the intensity of staining is shown on the X axis. (i) Quantification of the median intensity of lysotracker staining shows a mild but significant reduction in the proband in comparison to the father (n=3 flasks per individual, one-way ANOVA with Tukey's multiple comparison, father vs. proband P=0.0466). Error bars indicate mean +/- standard error of the mean.

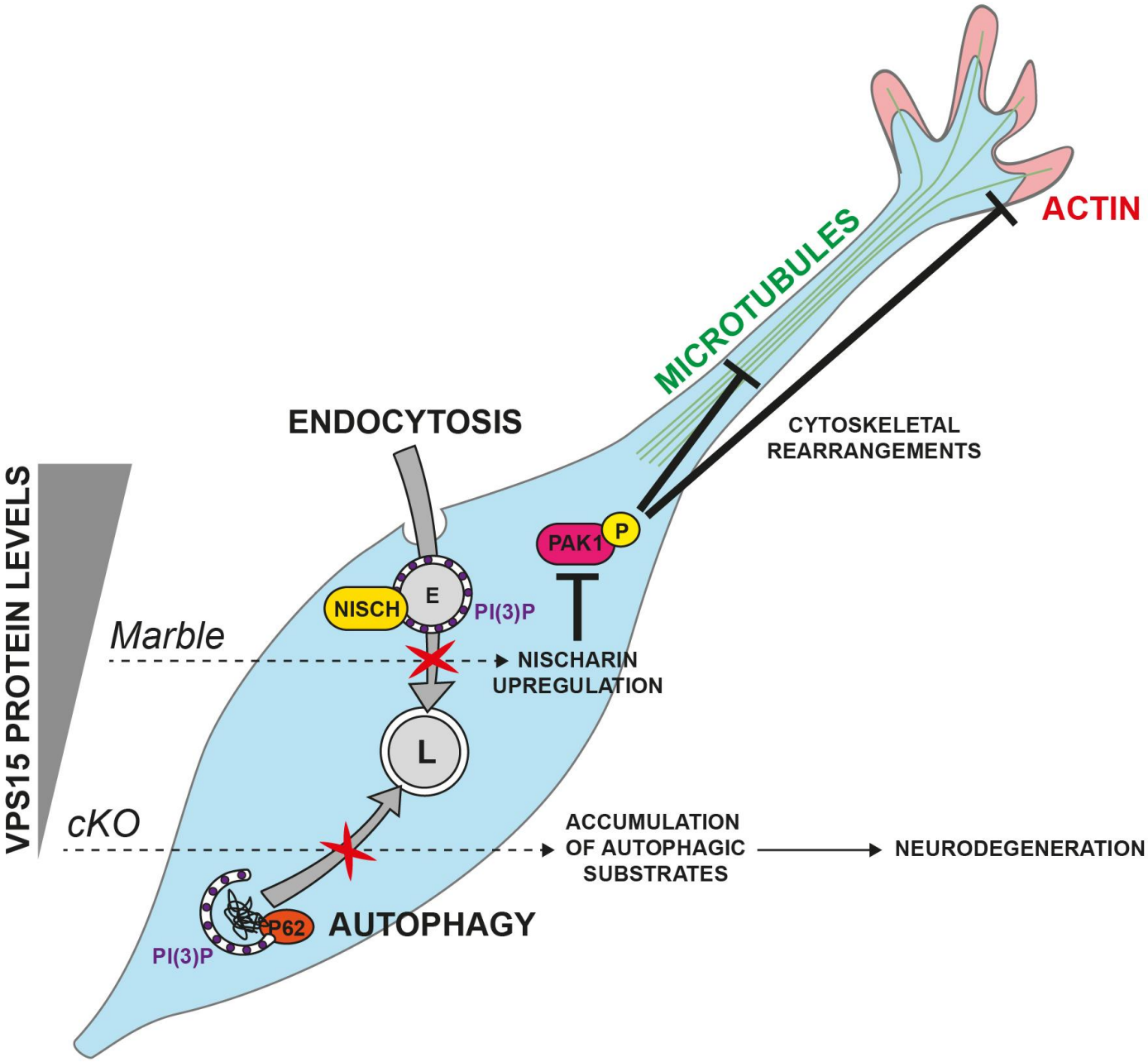

Supplementary Figure 10

Model showing the effect of *Vps15* mutations on neuronal migration and cell survival.

Under wild-type conditions Vps15 acts in a complex with Vps34 and Beclin1 catalyzing the formation of the phospholipid PI(3)P at endosomes and autophagosomes. The splice site mutation in the *Marble* mouse is a hypomorph, reducing the levels of the Vps15/Vps34 complex which impairs endosome (E) to lysosome (L) trafficking. As a consequence, Nischarin, a protein that binds PI(3)P and is localized to the endosome, is upregulated in *Marble* mutants. Nischarin inhibits Pak1 phosphorylation, which is known to influence microtubule dynamics through the phosphorylation of tubulin cofactor B and the actin cytoskeleton by activating LIM kinase. We propose that perturbation of this pathway causes the neuronal migration defect in *Marble* animals. If Vps15 is deleted in neurons, autophagy progression is blocked leading to the accumulation of p62 positive substrates. This in turn is associated with caspase induced cell death and severe cortical atrophy.

Figure 2a

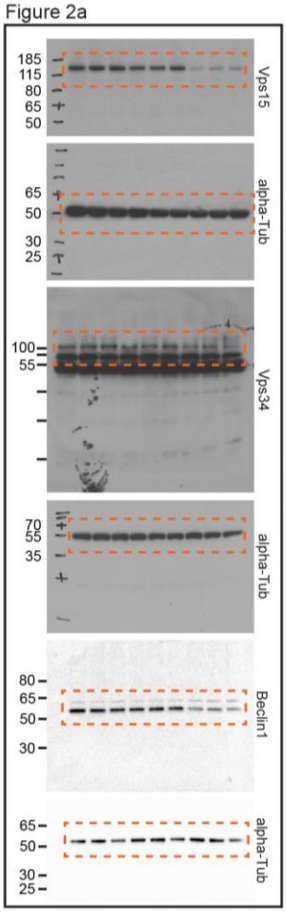

Figure 2c

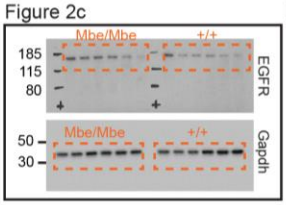

Figure 2e

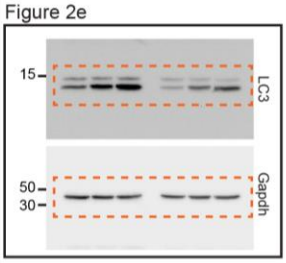

Figure 2i

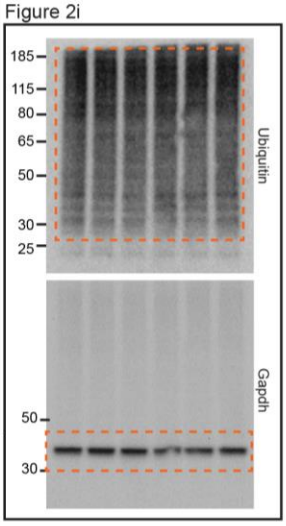

Figure 3d

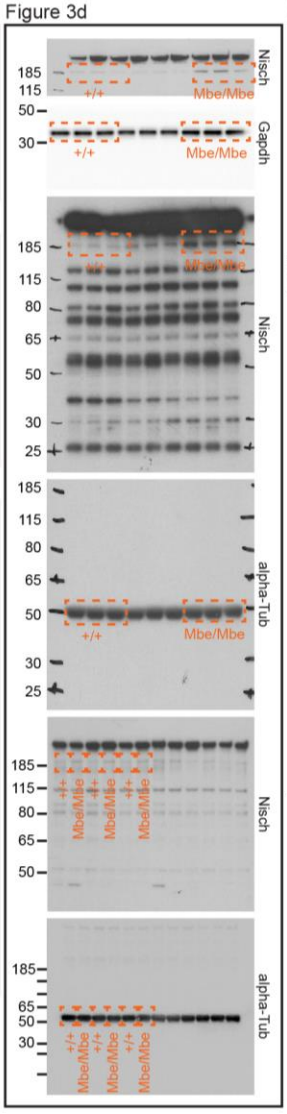

Figure 3g

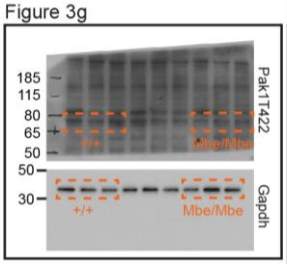

Figure 7e

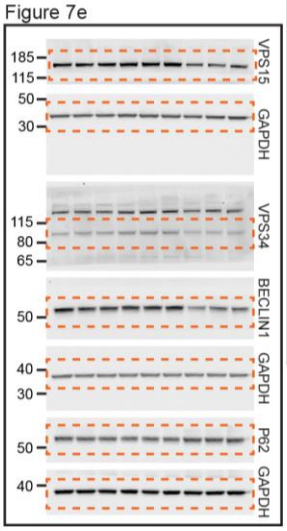

Figure 7j

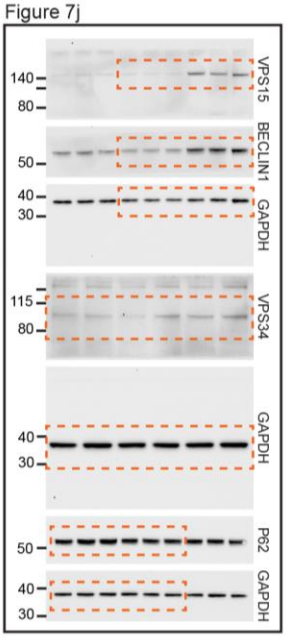

Supplementary Figure 2d

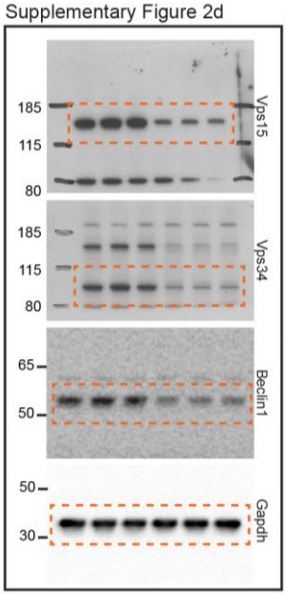

Supplementary Figure 2g

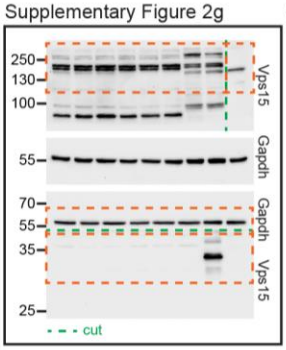

Supplementary Figure 7a

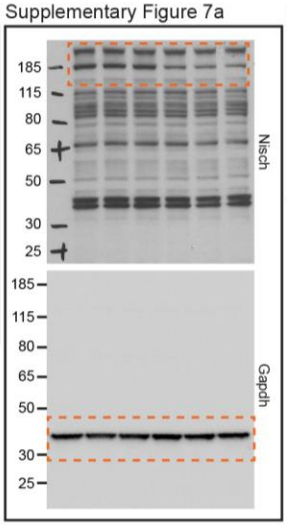

Supplementary Figure 9d

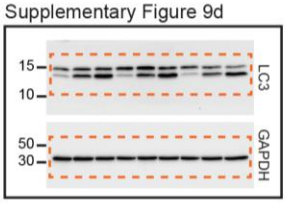

Supplementary Figure 11

Full scans of all western blots presented in this manuscript.

In some instances western blot membranes were cut allowing incubation with different antibodies. Shown are the full scans of each membrane fragment.